ADVANCED ENERGY & SUSTAINABILITY RESEARCH
www.advenergysustres.com

Fast and Facile Microwave Synthesis of Cubic $CuFe_2O_4$ Nanoparticles for Electrochemical CO_2 Reduction

*Judith Zander, Morten Weiss, and Roland Marschall**

Nanoparticles of cubic $CuFe_2O_4$ are obtained in a fast microwave-assisted hydrothermal synthesis. By adjusting the pH value and solvent ratio (ethylene glycol to water), phase purity and high crystallinity is achieved at very short reaction times of 1 min, or low temperatures of 120 °C, without the need for subsequent heat treatment steps. The influence of the synthesis time or temperature on material properties and performance in electrochemical CO_2 reduction to CO are investigated. While particle size and crystallinity are not changed significantly with longer synthesis times at 175 °C, prolonged heating results in a decrease of the degree of inversion, which leads to a decrease in the CO_2 reduction ability. The best performance is observed for $CuFe_2O_4$ with an intermediate degree of inversion of approx. 0.75, together with the largest crystallite size and micro-strain, as revealed by Rietveld refinement. For $CuFe_2O_4$ synthesized under these conditions, a CO evolution rate of 0.2 μmol h^{-1} g^{-1} is obtained at a Faradaic efficiency of 20%. The CO to H_2 ratio is 1:3, which makes it a promising candidate for a sustainable production of syngas.

1. Introduction

The combination of rising CO_2 concentrations in the atmosphere and the necessity for alternative production pathways of valuable carbon-containing chemicals have provoked an increasing interest in the capture and conversion of CO_2. Electrochemical CO_2 reduction is hereby especially promising, since it enables the direct conversion of electricity from renewable sources into chemical fuels, that can on the one hand serve as storage media to mitigate fluctuations in the power supply by renewables and on the other hand can be used as feedstock for industrial processes, such as Fischer–Tropsch, or the syntheses of valuable chemicals.[1–4] CO_2 reduction is a multielectron and frequently also a multiproton transfer reaction. This, together with the inert nature and the possibility of various reduction products, usually results in high required overpotentials and the occurrence of multiple reaction products.[5] The selectivity hereby strongly depends on the catalyst. Until recently, copper was the only metal electrocatalyst yielding CH_4 and higher carbon products, such as C_2H_4 or ethanol,[4] with Zhou et al. reporting in 2022 the production of linear and branched C_3 to C_6 hydrocarbons also over polarized $Ni^{\delta+}$ associated with Ni–O bonds.[6] Copper-containing materials, especially oxides, are likewise of interest due to their comparatively high activity and broad substrate scope. Copper oxides, such as CuO or Cu_2O, are reduced to metallic copper at the surface under operating conditions.[7–10]

Another interesting copper oxide is $CuFe_2O_4$ that only contains abundant iron as an additional element. $CuFe_2O_4$ belongs to the class of spinel-type materials that are normally of cubic crystal structure with the space group $Fd\bar{3}m$. However, due to the strong Jahn–Teller distortions induced by Cu^{2+}, lowering of the symmetry to tetragonal is favored at lower temperatures.[11] A cubic structure is stable above around 400 °C.[11,12] Spinels are of high interest also due to their magnetic and electronic properties, which can be adjusted by the degree of inversion, i.e., the cation distribution between tetrahedral and octahedral sites, and in the special case of $CuFe_2O_4$ also by the structure.[13–16] The degree of inversion influences the structure due to the strong Jahn–Teller distortion caused by Cu^{2+} at octahedral sites.[17] The exact relationship between structure and inversion parameter is, however, debated. A completely inverted structure was reported for cubic $CuFe_2O_4$ based on neutron diffraction results, with a slight reduction of the inversion parameter by a few percent upon phase transition to tetragonal.[18] On the other hand, a strong correlation between phase transition and cation migration is commonly believed to be present.[13–15,19] Thus, Ohnishi et al. observed a normal cation distribution for $CuFe_2O_4$ in the high-temperature cubic form. Copper migration to octahedral sites proceeds during cooling between approx. 700 and 360 °C, where the stronger Jahn–Teller distortion causes the transition to tetragonal and results in a strong correlation between inversion parameter and structure.[11–14,19–21] Cubic $CuFe_2O_4$ was reported as a normal spinel[19,20] as well as inverted.[11] The critical inversion

J. Zander, M. Weiss, R. Marschall
Department of Chemistry
University of Bayreuth
Universitätsstraße 30, 95447 Bayreuth, Germany
E-mail: roland.marschall@uni-bayreuth.de

J. Zander, R. Marschall
Bavarian Center for Battery Technology (BayBatt)
University of Bayreuth
Universitätsstrasse 30, 95447 Bayreuth, Germany

The ORCID identification number(s) for the author(s) of this article can be found under https://doi.org/10.1002/aesr.202200184.

© 2023 The Authors. Advanced Energy and Sustainability Research published by Wiley-VCH GmbH. This is an open access article under the terms of the Creative Commons Attribution License, which permits use, distribution and reproduction in any medium, provided the original work is properly cited.

DOI: 10.1002/aesr.202200184

© 2023 The Authors. Advanced Energy and Sustainability Research published by Wiley-VCH GmbH

parameter for phase transition is believed to be 0.75.[19] The cation distribution is largely dependent on the synthesis conditions, such as particle size and calcination temperature,[11,21–23] that appear to have the most significant impact on both structure and degree of inversion. Calculations have shown that the cation distribution significantly affects the electronic properties, with a change from a completely inverted structure to a normal one resulting in a change from semi-conducting to half-metallic properties.[19,24] This has experimentally been observed by a reduced grain resistance and improved conductivity for partially inverse tetragonal $CuFe_2O_4$ compared to normal cubic $CuFe_2O_4$.[19]

$CuFe_2O_4$ has been used for several catalytic processes, such as methanol steam reforming,[22] photocatalytic degradation,[23] photocatalytic water splitting,[25] photoelectrochemical hydrogen evolution,[26] photoelectrochemical water oxidation,[27,28] as well as gas sensor material[29] or for protein separation.[30] A huge advantage is the easy recovery of the material due to its magnetic properties. Additionally, $CuFe_2O_4$ is an effective electrocatalyst for oxygen evolution, for which it showed a very low overpotential, even surpassing the performance of $CoFe_2O_4$ and $NiFe_2O_4$.[31] $CuFe_2O_4$ has also been used for the photoelectrochemical (PEC) CO_2 reduction reaction (CO_2RR).[32,33] Thus, the group of Khan first employed pure $CuFe_2O_4$ for PEC CO_2RR to methanol and then switched to a composite with graphene oxide, thereby increasing the Faradaic efficiency to 87%, reportedly due to better charge separation.[32,33] Improved activity —also for the conversion to methanol—could also be observed for a composite with TiO_2, as reported by Hafeez et al.[34]

Common synthesis methods include co-precipitation,[29] solid-state reaction,[11,19] sol–gel synthesis,[31] combustion synthesis,[35] or solvothermal synthesis.[30,36] Methods requiring calcination temperatures of more than 300 °C yield tetragonal $CuFe_2O_4$, if cooled slowly, and cubic, if quenched rapidly from high temperatures. Additionally, most of these techniques yield large particle sizes, with inhomogeneous size distributions and low surface areas because of the high temperature requirements, which is often impedimental for catalytic performance.[22] To obtain nanosized or nanostructured particles, different strategies, such as hard templating, soft templating, or combustion synthesis, can be employed.[22,23,35] In contrast to solid-state synthesis, hydrothermal synthesis allows for the direct preparation of the cubic form.[36] As an alternative, microwave-assisted syntheses allow for the preparation of spinel ferrite nanoparticles.[37–39] Due to fast homogeneous heating, reaction times can often be significantly reduced compared to conventional hydrothermal synthesis and the size distribution can be narrowed.[37,38,40–42] Phuruangrat et al. have shown in first experiments that microwave-assisted hydrothermal synthesis is feasible for the direct synthesis of crystalline $CuFe_2O_4$ in its cubic form.[43] Jalajerdi et al. obtained tetragonal $CuFe_2O_4$ after an aqueous microwave synthesis followed by calcination.[44] The size distribution is relatively broad, however. To improve the size distribution of nanoparticles, triethylene glycol (TEG) has been used as a solvent in a solvothermal synthesis of $CuFe_2O_4$ nanorods, serving as reducing agent, high boiling solvent, and stabilizer.[45] Similar approaches with the solvent acting as a stabilizing agent have been shown for other ferrites in our group as well.[37–39] For copper ferrite, a microwave synthesis in organic solvents, however, results in a reduction of Cu^{2+} and the formation of Cu^0 by-phases.[41]

We herein present a fast, reproducible microwave-assisted synthesis of cubic $CuFe_2O_4$ nanoparticles in water, with additional ethylene glycol acting as stabilizing agent in the reaction solution, improving phase purity and homogeneity by preventing the precipitation of hydroxides. We further examine the influence of synthesis parameters on the material properties, the degree of inversion, and on the activity in electrochemical CO_2 reduction. The best performance is observed for $CuFe_2O_4$ with an intermediate degree of inversion, for which a CO evolution rate of $0.2\,\mu mol\,h^{-1}\,g^{-1}$ was obtained at a Faradaic efficiency of 20%. The CO to H_2 ratio was 1:3.

2. Results and Discussion

The synthesis of $CuFe_2O_4$ in water is strongly pH-dependent, which was also observed for a hydrothermal synthesis approach.[36] Fe_2O_3 was the only reaction product observed in the XRD patterns under acidic conditions, CuO was the main product at near neutral conditions, and $CuFe_2O_4$ was only observed at pH > 10 (Figure S1, Supporting Information). In contrast to Phuruangrat et al., we observed CuO occurring as by-phase in varying amounts when the synthesis was conducted in pure water, especially at a pH below 12 (Figure S1, Supporting Information). This is likely due to the precipitation of hydroxides upon pH adjustment before transfer to the microwave, which results in visibly inhomogeneous mixing. Upon addition of ethylene glycol as a complexing agent, which optically improved the dispersion, the synthesis reproducibly yielded phase-pure cubic $CuFe_2O_4$ at medium amounts of ethylene glycol (EG). If the amount of EG exceeded 40%, a reduction of copper was observed (Figure S2, Supporting Information), in good agreement to the results reported by Solano et al.[41] The best results were obtained using a EG:water ratio of 5:10 (1:2).

After having established the general reaction parameters, we varied the reaction time and temperature for the microwave synthesis. The corresponding XRD patterns are depicted in **Figure 1** and S3, Supporting Information. A reduction of the synthesis time to only 1 min was possible, without the appearance of any by-phases and without apparent loss of crystallinity. A similar reduction of the synthesis time to 1 min could additionally be shown at 150 °C (Figure S4, Supporting Information). The employed synthesis temperature has a stronger influence on crystallinity and phase purity. While the distinct reflections for cubic $CuFe_2O_4$ are apparent even after reaction at only 120 °C for 15 min, the crystallinity was low and a shoulder to the left of the (311) reflection indicated the presence of a possible tetragonal phase. When the temperature was raised to 200 °C, Cu_2O by-phases were observed in high-resolution Ag-XRD patterns (Figure 1 and S3, Supporting Information), likely due to the strong reducing ability of EG at this temperature. The crystallite sizes for $CuFe_2O_4$ obtained after different reaction times, as well as at different temperatures, were first calculated by the integral breadth method and additionally by Rietveld refinement due to the high background (Figure 1c,d). The prominent background could be an indication of an amorphous phase that probably corresponds to organic residues. Both methods yield a crystallite size of 10–13 nm, depending on the reaction time. A correlation with the degree of inversion was noted and is discussed in the

© 2023 The Authors. Advanced Energy and Sustainability Research published by Wiley-VCH GmbH

26999412, 2023, 4, Downloaded from https://onlinelibrary.wiley.com/doi/10.1002/aesr.202200184 by Universitaet Bayreuth, Wiley Online Library on [24/07/2023]. See the Terms and Conditions (https://onlinelibrary.wiley.com/terms-and-conditions) on Wiley Online Library for rules of use; OA articles are governed by the applicable Creative Commons License

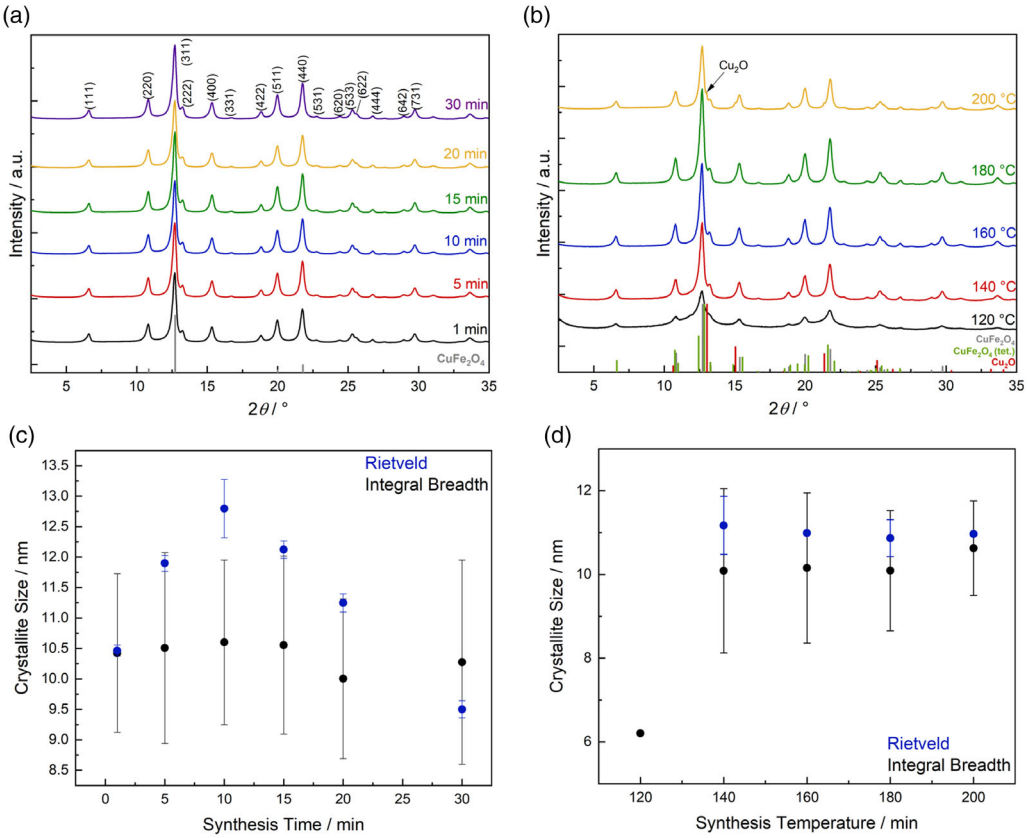

Figure 1. Ag-XRD patterns for $CuFe_2O_4$ obtained after different reaction temperatures at 175 °C a) and after 15 min at different reaction times b). Following ICDD reference patterns were used: $CuFe_2O_4$ (c): 01-077-0010; $CuFe_2O_4$ (*t*): 00-034-0425, Cu_2O: 00-005-0667. Crystallite sizes obtained via the integral breadth method and Rietveld refinement are depicted in c) and d). Error bars for the integral breadth method are estimated by averaging over different reflections in the cubic structure; error bars for sizes derived from Rietveld analysis indicate averaging of at least two independent fits.

following sections. A significantly smaller crystallite size of only approx. 6.5 nm was estimated after the reaction proceeded at 120 °C, whereas the crystallite size remains unchanged for increasing reaction temperatures. The determination of crystallite size by the integral breadth method for the 120 °C sample was only possible for the (400) reflection due to low crystallinity and peak overlap. For the same reasons, Rietveld refinement did not result in a good fit.

SEM images show the agglomeration of very small nanoparticles (Figure S5, Supporting Information) that have an almost perfect Cu:Fe ratio of 0.5 determined by EDXS. For further evaluation of the synthesis parameters on the crystal morphology, the obtained particles were analyzed with TEM (**Figure 2** and S6, Supporting Information). Slightly increasing particle sizes with increasing synthesis time were estimated, with the particles growing from approx. 13.5 to 18.5 nm. Similar sizes were obtained after reaction at temperatures between 140 and 180 °C as well (Figure S6, Supporting Information), with the size increasing from 14 to 18 nm. The average particle size is only slightly larger than the determined crystallite size, indicating that the nanoparticles are mostly single crystalline. The crystallinity and cubic structure were further confirmed by measuring lattice spacing in high-resolution images (Figure S5, Supporting Information). The spacing corresponding to the (311)-plane in the cubic structure was the most prominent one.

The surface area was evaluated by the BET model. The surface area of $CuFe_2O_4$ particles synthesized at a fixed temperature of 175 °C is around 120 $m^2\,g^{-1}$, independent of the synthesis time (Figure S7, Supporting Information). The corresponding isotherms have the typical shape for nanoparticle agglomerates, revealing that the high surface area is a result of the small size of the obtained nanoparticles. Correspondingly, no defined pore size is observed, and the void size between nanoparticles peaks around the particle diameter. The particles obtained after shorter reaction times exhibit a tendency to form agglomerates with smaller voids, possibly due to organic residues and very small amorphous compounds. The similar surface area independent of the size is in good agreement to the similar sizes observed in the TEM images. The surface area for particles obtained after reaction at different temperatures decreases with increasing reaction temperature from 250 to 100 $m^2\,g^{-1}$, although the particle size was very similar. This might be an indication of different agglomeration behavior that is also apparent in different shapes of the isotherms and might either depend on the amount of organic residues or on different magnetic properties. The packing of nanoparticles is much denser for samples synthesized at low temperature (i.e., 120 or 140 °C), which show a narrow pore size distribution that peaks around 5 nm (Figure S7, Supporting Information). The dense packing is furthermore hinted at in the

© 2023 The Authors. Advanced Energy and Sustainability Research published by Wiley-VCH GmbH

26999412, 2023, 4, Downloaded from https://onlinelibrary.wiley.com/doi/10.1002/aesr.202200184 by Universitaet Bayreuth, Wiley Online Library on [24/07/2023]. See the Terms and Conditions (https://onlinelibrary.wiley.com/terms-and-conditions) on Wiley Online Library for rules of use; OA articles are governed by the applicable Creative Commons License

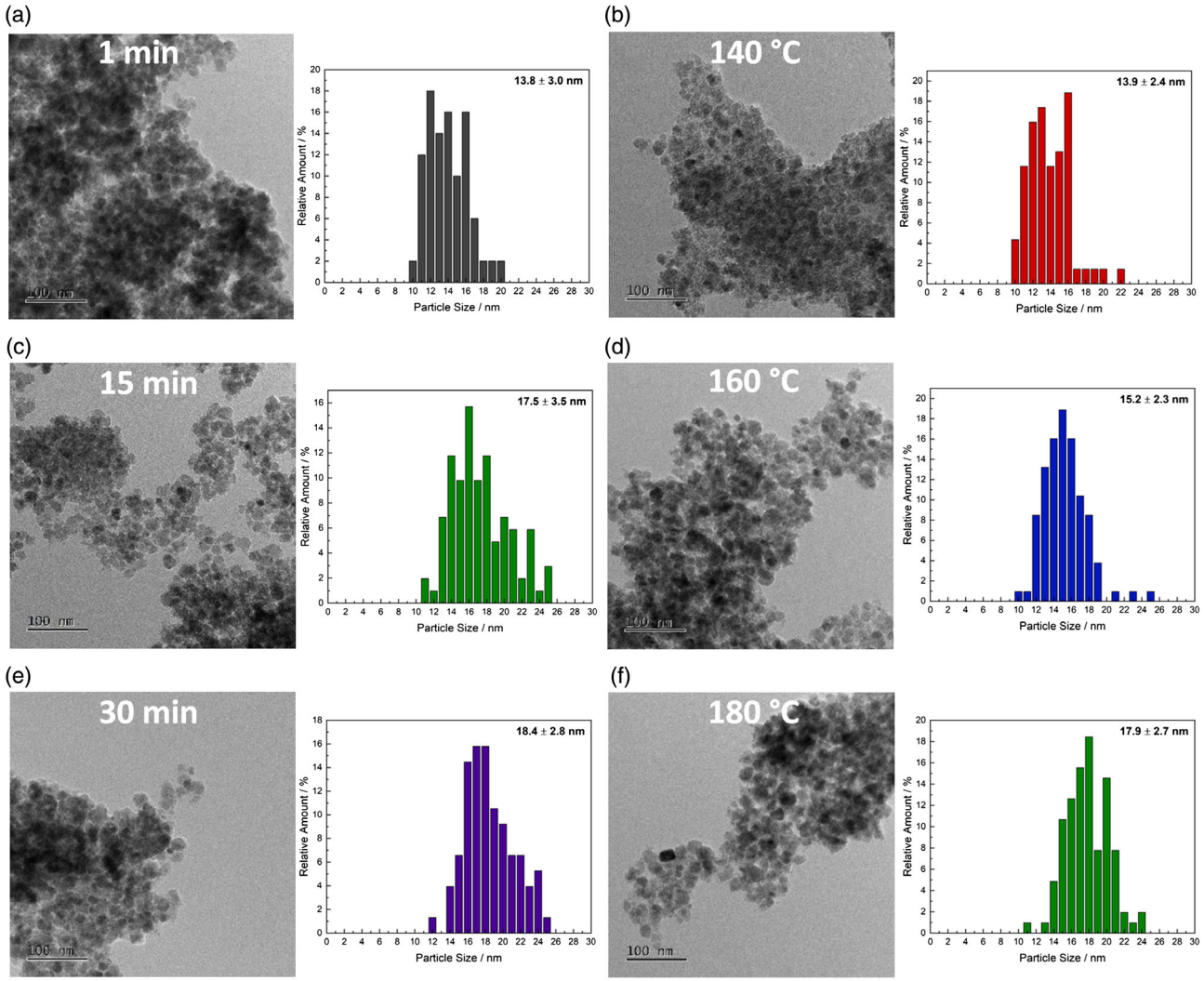

Figure 2. TEM images of $CuFe_2O_4$ particles obtained after different reaction times at 175 °C a,c,e) and after 15 min at different reaction temperatures b,d,f), as well as corresponding particle size distribution. For the determination of size distributions, at least 50 particles were measured.

TEM images. Larger amounts of organic residues or amorphous matter might contribute to void filling between particles. The BET surface area for $CuFe_2O_4$ obtained after different reaction times at 150 °C is around 150 $m^2\,g^{-1}$, thus larger than for the particles prepared at 175 °C, which is in good agreement to the increased surface area at lower temperatures mentioned above.

To evaluate whether the differences in the agglomeration behavior are due to organic residues on the surface, TG-MS measurements were conducted for $CuFe_2O_4$ obtained after different reaction times or at different temperatures (**Figure 3**). As expected, the mass loss during annealing in air increases with decreasing reaction times. An initial increase of the mass below 100 °C can probably be attributed to oxidation of organic matter, likely followed by a loss of adsorbed H_2O at approx. 125 °C and decomposition of organic matter mainly into CO_2 at 150 to 350 °C (Figure S9, Supporting Information). A similar effect is observed for samples obtained after different reaction times, with the mass loss being even more pronounced for $CuFe_2O_4$ synthesized at lower temperatures, with the sample synthesized at 120 °C showing a mass loss of 15%.

The higher amounts of organic residues might explain the increased surface area for samples obtained at low temperatures. Corresponding to the decomposition of organic residues, exothermic peaks can be observed in the DSC measurements (Figure S9, Supporting Information). Additionally, two steps with increasing heat flow are visible, one between 300 and 400 °C and one between 620 and 700 °C. Those features might correspond to phase transitions, first from cubic to tetragonal and later from tetragonal to cubic. The onset temperature for the first phase transition shifts toward higher temperatures with increasing synthesis duration and the increase in the heat flow decreases. Both might be an indication of different initial cation distributions.

The organic residues are also apparent in the DRIFT spectra for all samples (Figure 3c,d, S9, Supporting Information). Additionally, differences between samples obtained after different

© 2023 The Authors. Advanced Energy and Sustainability Research published by Wiley-VCH GmbH

26999412, 2023, 4, Downloaded from https://onlinelibrary.wiley.com/doi/10.1002/aesr.202200184 by Universitaet Bayreuth, Wiley Online Library on [24/07/2023]. See the Terms and Conditions (https://onlinelibrary.wiley.com/terms-and-conditions) on Wiley Online Library for rules of use; OA articles are governed by the applicable Creative Commons License

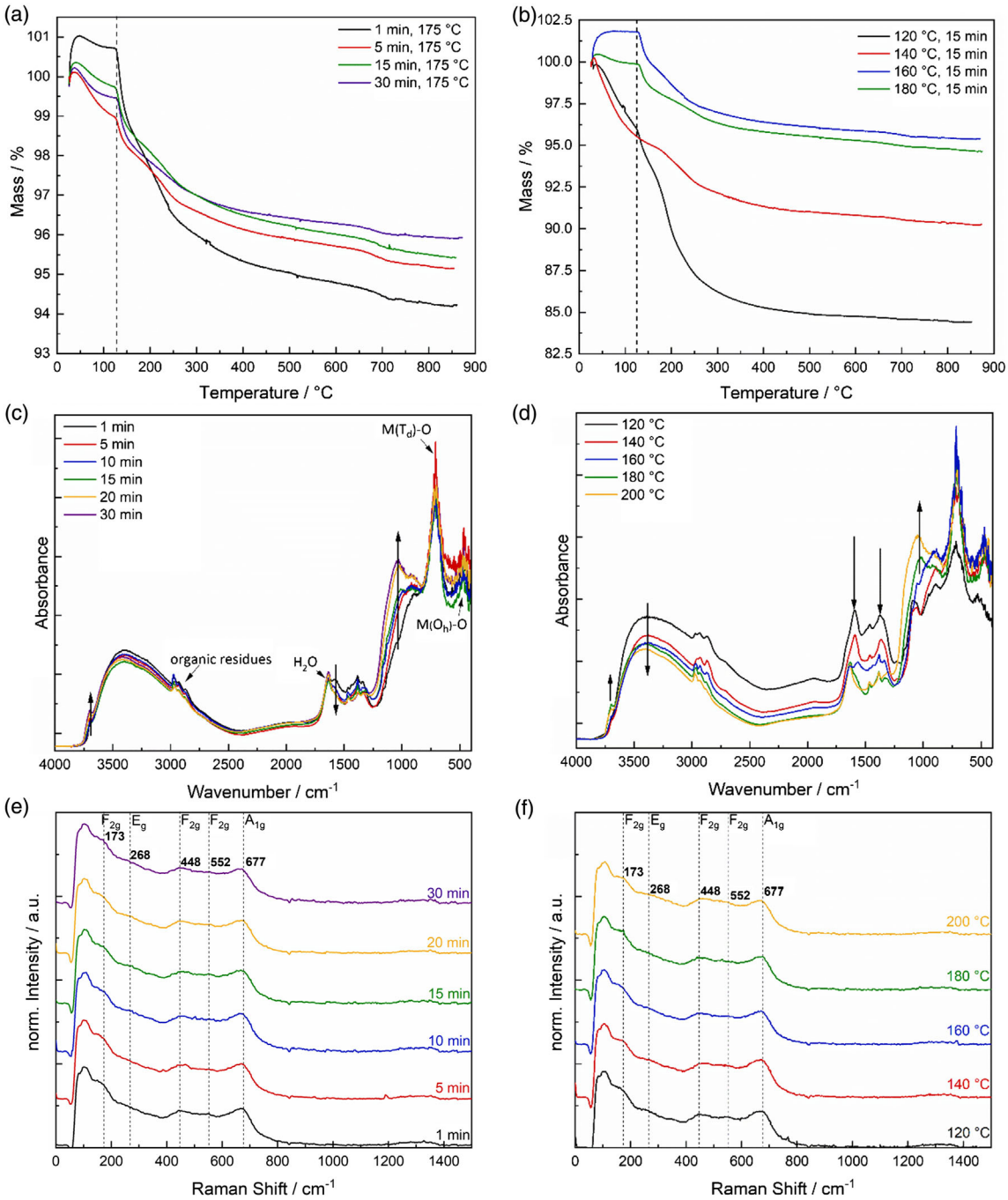

Figure 3. Observed mass loss during annealing of $CuFe_2O_4$ particles obtained after reaction for different duration at 175 °C a), or for 15 min at different temperatures b), DRIFT spectra for $CuFe_2O_4$ synthesized under varied conditions c,d), as well as corresponding Raman spectra e,f).

reaction times, or at varied temperatures, are apparent, indicating structural changes that are not visible in the XRD patterns and thus do not significantly influence the crystallinity. All samples exhibit the characteristic absorbance at 400–550 cm^{-1} corresponding to metal–oxygen vibrations at octahedral sites, ν_2, and the absorbance between 620 and 750 cm^{-1}, ν_1, corresponding to metal–oxygen vibrations at tetrahedral sites.[46–49] The vibrations show only negligible changes in dependence of the synthesis time or temperature, indicating a complete condensation of metal–oxygen bonds even at short times and low temperatures, in good agreement to highly similar XRD patterns. An exception is $CuFe_2O_4$ synthesized at only 120 °C, for which the M–O vibrations are less intense, likely due to incomplete condensation to the oxide. Correspondingly, a larger amount of hydroxyl-groups is observed between 3000 and 3500 cm^{-1} in addition to organic residues from ethylene glycol and its decomposition products.[45] Noticeably, the

© 2023 The Authors. Advanced Energy and Sustainability Research published by Wiley-VCH GmbH

26999412, 2023, 4, Downloaded from https://onlinelibrary.wiley.com/doi/10.1002/aesr.202200184 by Universitaet Bayreuth, Wiley Online Library on [24/07/2023]. See the Terms and Conditions (https://onlinelibrary.wiley.com/terms-and-conditions) on Wiley Online Library for rules of use; OA articles are governed by the applicable Creative Commons License

intensities of the vibrational bands at 1030 cm^{-1}, corresponding to COH-bonds in poly-ethylene glycol, and at 3690 cm^{-1}, corresponding to non-hydrogen bonded OH, increase with the synthesis time, while those at 1380 and 1330 cm^{-1}, that fall into the range of C-O bonds, decrease slightly.[50] An observed decrease of the vibration at 1585 cm^{-1} and increase of the vibration at 1030 cm^{-1} are similar to evolutions observed during the polymerization of ethylene glycol that might occur as a side reaction.[51] Additional weak absorption bands between 1050 and 1160 cm^{-1}, which are especially visible at short reaction times or low temperatures, might also be attributed to C–O in ethylene glycol residues.[45] A similar trend is visible with increasing reaction temperature, if more pronounced.

Raman spectra were recorded for $CuFe_2O_4$ obtained under varying synthesis conditions to corroborate the cubic structure and phase purity deduced from the XRD patterns (Figure 3e,f). The visible bands for all samples can be assigned to the 5 expected Raman active modes for cubic $CuFe_2O_4$ and are in good agreement to literature values.[47,52] No characteristic bands for common by-phases, such as Fe_2O_3, are visible. The band at a shift of 173 cm^{-1} is assigned to the F_{2g} mode, that at 268 cm^{-1} to E_g, that at 448 cm^{-1} and 553 cm^{-1} to F_{2g} as well, and that at 677 cm^{-1} to the A_{1g} mode.[47] Additional humps at 350 cm^{-1} and a shoulder at 620 cm^{-1} might be an indication of locally lowered symmetry due to Jahn–Teller distortions caused by Cu^{2+} ions in an octahedral environment, although a universal distortion of the crystal lattice is not apparent in the XRD patterns. A similar observation has been stated by Silva et al. for co-substituted $CuFe_2O_4$.[47] However, additional bands might also be formed due to partial inversion that also lowers the symmetry.[16] Due to the weak intensity of those bands, no clear conclusion about the local environment of Cu and Fe ions, in terms of phase transformation and degree of inversion, can be drawn from the DRIFT and Raman spectra, however.

For further characterization of the as-synthesized nanoparticles, UV/vis/NIR measurements were conducted in order to estimate the bandgaps. Irrespective of the synthesis conditions, a bandgap of approx. 1.9–2.0 eV was obtained from the Kubelka–Munk plots, in good agreement to literature values (Figure S10, Supporting Information).[27,28,53] Since the bandgap is highly dependent on the degree of inversion, similar cation distribution independent of the synthesis conditions can be assumed.[19] A feature at 485 nm is apparent in the spectra, corresponding to ligand to metal charge-transfer from oxygen to copper 3*d* orbitals. If this region is ignored in the fit, slightly lower values were obtained, compared to a fit only above the *d*–*d* band (Figure S10, Supporting Information). A second, weak feature at approx. 800 nm can be attributed to *d*–*d* transitions in Cu^{2+} at distorted octahedral sites. A third, very weak feature centered around 1500 nm arises due to *d*–*d* transitions in Cu^{2+} at tetrahedral sites.[54–56] Bandgap values were also determined from the Tauc plots that yield a bandgap of 1.7–1.8 eV for an indirect transition that includes a fit over the *d*–*d* band and thus leads to a slight underestimation of the bandgap, and of 2.5 eV for a direct transition, that allows for an exclusion of the *d*–*d* band for the fit. From the shape of the plots and the estimated bandgap values, an indirect bandgap is more probable, although this is in discrepancy to the result of the group of Sivula.[27] However, they used n-type, tetragonal thin-film $CuFe_2O_4$, which might exhibit considerably alternate properties. The results of Díez-García et al. for cubic $CuFe_2O_4$ are rather more similar to ours.[53] Notably, the *d*–*d* band is hardly visible in both reported spectra.

2.1. Determination of the Degree of Inversion

Generally, three main methods are employed to determine the degree of inversion for spinel-type materials: Rietveld refinement of XRD data, Mössbauer spectroscopy, and XPS.[16,31] Since all three rely on mathematical fitting of experimental results and thus depend on the quality of the measurement data and the fitting parameters, a complementary determination with several methods is recommendable. We performed Rietveld refinement on the Cu and Ag-XRD patterns for $CuFe_2O_4$ obtained under different conditions. The high background due to organic residues, low intensity and broad, asymmetric peak shape make an unambiguous fitting difficult due to strong correlations between occupation, background, asymmetry, micro-strain, and anisotropic size parameters. A degree of inversion between 0.72 and 0.87 was estimated for all samples based on the Cu-XRD data, depending on the fitting conditions (Figure S12, Supporting Information). This is in good agreement to the usually observed value of 0.85 at room temperature, although a tetragonal distortion would normally be expected.[15,21,23,24,57] The degree of inversion decreases with increasing reaction time, signifying that although crystallization mainly occurs during the first minute of the synthesis, continued microwave irradiation induces a Cu^{2+} migration to tetrahedral sites. The very fast heating and crystallization, together with an abrupt stop in the microwave irradiation—i.e., the apparent driving force for cation redistribution—lead to the thermodynamically unfavorable structure and prevent the distortion that is usually observed during the cooling from high temperatures.

Interestingly, a closer look at the crystallite sizes determined with the integral breadth method and Rietveld refinement reveals that the size is highest after medium synthesis times of 10 min, suggesting that crystallinity is decreasing again after that time (Figure 1). This goes in hand with a pronounced decrease in the inversion parameter, as discussed in the following, indicating that microwave-induced cation redistribution results in an increasing structural disorder. A closer analysis of the crystallite size derived from different reflection peaks reveals that the observed relationship is at least partially an effect of averaging for different (hkl) reflections. All samples show an average crystallite size of approx. 11 nm when analyzed with the integral breadth method, but the differences between the determined sizes are largest for very short or very long reaction times, with the smallest deviations observed for $CuFe_2O_4$ obtained after a reaction time of 10 min (Figure S11, Supporting Information). The same trend as for the crystallite size can be observed for micro-strain, while the lattice parameter is slightly smaller for $CuFe_2O_4$ obtained after moderate reaction times, indicating lattice contraction (Figure S11, Supporting Information). Both effects can be a result of Jahn–Teller distortions that would, if in equilibrium, likely result in a tetragonal structure. On the one hand, the strain induced by Jahn–Teller active Cu^{2+} ions on octahedral sites depends on the degree of inversion and would be expected to decrease with a decreasing degree of inversion.

© 2023 The Authors. Advanced Energy and Sustainability Research published by Wiley-VCH GmbH

26999412, 2023, 4, Downloaded from https://onlinelibrary.wiley.com/doi/10.1002/aesr.202200184 by Universitaet Bayreuth, Wiley Online Library on [24/07/2023]. See the Terms and Conditions (https://onlinelibrary.wiley.com/terms-and-conditions) on Wiley Online Library for rules of use; OA articles are governed by the applicable Creative Commons License

This effect is most probably the reason for the decrease in micro-strain and crystallite size for samples obtained at reaction times longer than 10 min, in correlation to a decreasing inversion parameter. Notably, the degree of inversion is around 0.75, or less, after this time. This value represents the critical fraction of Cu^{2+} on octahedral sites above which a distortion was observed in literature.[19] The increasing differences in peak width for different hkl at increasing temperature might be an effect of anisotropic disorder induced by cation migration. For the sample obtained after 30 min, no accurate determination of the degree of inversion was possible. An increase in micro-strain was obtained for different fitting procedures. Possibly, cation migration results not only in the induction of disorder but also causes additional strain effects due to inhomogeneous ion distribution in different unit cells and to the creation of defects. Since micro-strain and crystallite size are low for the samples obtained after short reaction times, the presence of defects—due to partially incomplete condensation of the metal-oxide framework—might mitigate strain induced by Jahn–Teller distortions. Additionally, at a degree of inversion of 0.75, the Jahn–Teller distortion at tetrahedral sites (that would result in a decrease of $c/a < 1$) and at octahedral sites (that would lead to $c/a > 1$) might compensate each other best, resulting in overall minimal distortion, but high strain.

The asymmetry of the reflections is even higher for the Ag-XRD data, hence we focused on measurements with a copper source for the fittings. The strong asymmetry of the reflections might in part be caused by internal stresses caused by the Jahn–Teller active Cu^{2+} ions.[11] A comparable, but slightly decreasing degree of inversion of around 0.8 was obtained for $CuFe_2O_4$ synthesized for 15 min at different temperatures. Summarized results for the cation distribution with an optimized fitting procedure are listed in **Table 1**.

XP spectra were recorded for $CuFe_2O_4$ synthesized at different temperatures or for different reaction times (**Figure 4**, S13, Supporting Information). The survey scans show the expected ratios for Cu and Fe, with additional small amounts of Si and K (Table S2, Supporting Information). The latter likely result from leaching of the microwave vial and the employed KOH, respectively. The concentration of K and Si increases with the synthesis time and temperature, indicating increasing amounts of doping with these ions. Additionally, the Cu content at the surface is decreased in the sample obtained after 30 min at 175 °C, further strengthening the assumption of defect induction due to increased cation migration with time. In contrast to that, a Cu excess at the surface was observed at high reaction temperatures. The Cu $L_3M_{4,5}M_{4,5}$ peak was used for charge correction, since non-negligible amounts of carbonaceous residues from the synthesis, which include significant contributions from alcoholic species to varying extents (Figure S13, Supporting Information), render a correction via adventitious carbon unsuitable and would result in vastly fluctuating binding energies. Typical binding energies for Fe^{3+} and Cu^{2+} of 933.1 eV for Cu $2p_{3/2}$ and 710.8 and 724.5 eV for Fe $2p_{3/2}$ and Fe $2p_{1/2}$ were observed, respectively. The high-resolution $2p$-spectra for Cu can be fitted with two signals for the metal ion in octahedral and tetrahedral sites, respectively.[23,31,32,58,59] This fitting approach is based on an influence of the coordination environment on the ratios of multiplet splitting,[58–60] but neglects additional effects on multiplet splitting and is further complicated by the possible presence of Cu^{+} and/or Cu^{0}. To some extent, the expected influence of Cu^{+}/ Cu^{0} can be derived from the Auger signal, which is highly similar for all $CuFe_2O_4$ samples obtained at 175 °C for different reaction times and supports the predominant oxidation state of +II for copper, which is further apparent in the high shake-up intensity.[61] No indication of Cu^{0} species is observed in the Cu $L_3M_{4,5}M_{4,5}$ spectra. Samples obtained at different temperatures, on the other hand, show a strong contribution of Cu^{+}, with the Cu^{+}/Cu^{2+} ratio depending on the synthesis temperature (Figure 4, S13, Supporting Information). Interestingly, although Cu^{+} by-phases were only observed at very high temperatures, the Cu^{+} content increases with decreasing reaction temperature, indicating partially reduced and likely also coordinative unsaturated copper species at the surface. The amount of Cu_2O in the sample obtained at 200 °C is estimated to be 1.2% based on the results from Rietveld refinement. The degree of inversion is clearly changing with prolong reaction times. While an initial 16% of Cu^{2+} on tetrahedral sites is observed after a very short reaction time of 1 min, an increasing amount of 33% of Cu^{2+} is located at tetrahedral sites after 30 min, in good agreement to the results obtained from Rietveld refinement. Interestingly, the degree of inversion as determined via Rietveld refinement shows an almost linear decrease after 10 min of reaction time. An extrapolation of that trend would yield a degree of inversion of approx. 0.66 for the sample obtained after 30 min, which is in very good agreement to the degree of inversion determined with XPS. A similar degree of inversion of $\lambda = 15$–20% is obtained independent of the synthesis temperature, with a slight decrease of the inversion parameter with increasing reaction temperature. The degree of inversion and the Cu^{+}/Cu^{2+} ratio are summarized in Table 1. Evolution of the degree of inversion and the Cu^{+}/Cu^{2+} ratio in relation to the synthesis time and temperature, respectively, are furthermore clearly demonstrated in the normalized spectra (Figure 4).

A similar fitting procedure should in theory also be possible for the Fe $2p$ spectra, but due to the more complicated multiplet structure, an overlap with a Cu Auger signal and low intensity of the peaks, an unambiguous fitting with only two species for Fe at tetrahedral and at octahedral voids is often neither possible nor meaningful and was therefore not attempted here.[58,59] The Fe $2p$ spectra were instead fitted with typical peak ratios and positions for ferrites, keeping the positions fixed for all samples.[62] When regarding the normalized Fe $2p$ spectra, interestingly a peak broadening toward higher binding energies is observed

Table 1. Degree of inversion (λ) determined with Rietveld refinement and XPS analysis.

Synthesis time	λ Rietveld	λ XPS	Cu^{+}/Cu^{2+}	Synthesis temperature	λ Rietveld	λ XPS	Cu^{+}/Cu^{2+}
1 min	0.82	0.84	0.02	120 °C		0.86	1.42
5 min	0.82	0.82	0	140 °C	0.87	0.87	0.08
10 min	0.80	0.78	0.02	160 °C	0.86	0.75	0.05
15 min	0.75	0.80	0.02	180 °C	0.79	0.81	0.03
20 min	0.72	0.78	0	200 °C	0.77	0.80	0.03
30 min	0.87	0.67	0.08				

© 2023 The Authors. Advanced Energy and Sustainability Research published by Wiley-VCH GmbH

26999412, 2023, 4, Downloaded from https://onlinelibrary.wiley.com/doi/10.1002/aesr.202200184 by Universitaet Bayreuth, Wiley Online Library on [24/07/2023]. See the Terms and Conditions (https://onlinelibrary.wiley.com/terms-and-conditions) on Wiley Online Library for rules of use; OA articles are governed by the applicable Creative Commons License

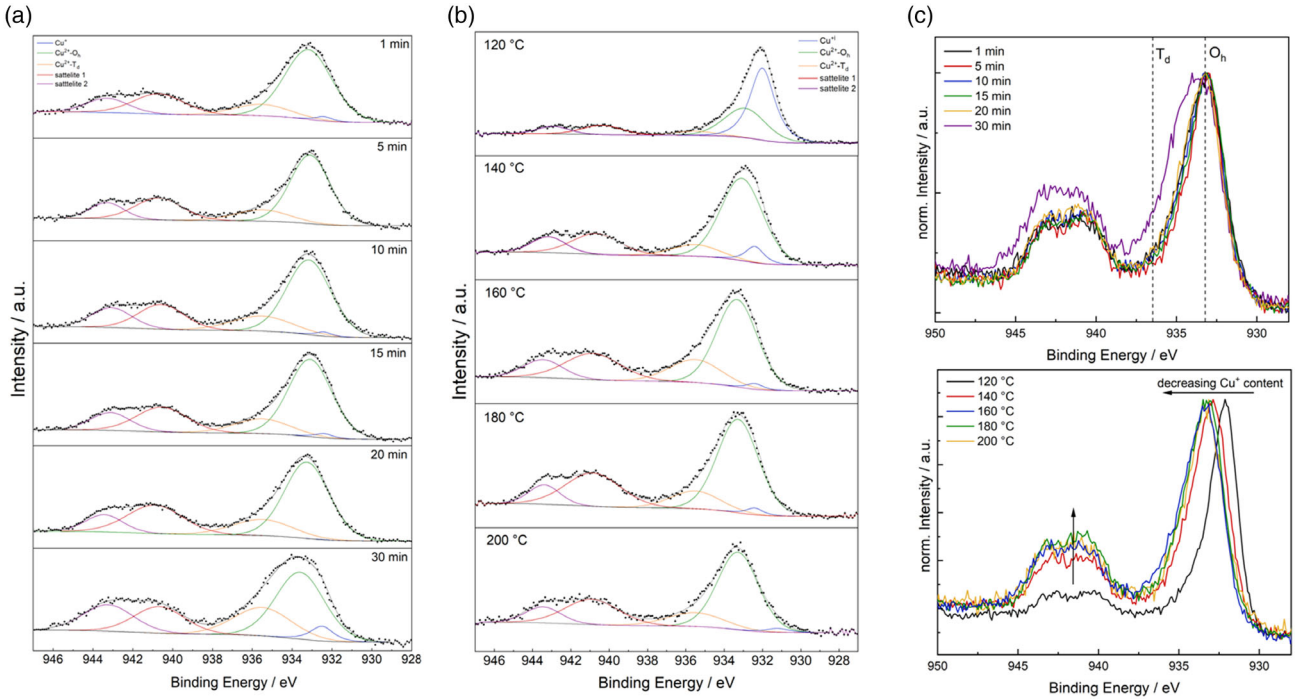

Figure 4. XPS spectra for $CuFe_2O_4$ obtained under different reaction conditions. Cu $2p_{3/2}$ spectra for $CuFe_2O_4$ synthesized at 175 °C for different reaction times a), or at different temperature b), as well as normalized $2p_{3/2}$ spectra c).

for samples obtained after 1 min and after 30 min, which would at first glance indicate a larger amount of Fe^{3+} in tetrahedral voids. For $CuFe_2O_4$ obtained after 30 min, this is additionally accompanied by a shift of the entire spectrum toward higher binding energies. This is contrary to the effects expected based on analysis of the Cu-spectra and on Rietveld refinement and could be an indication of independent cation migration of Cu and Fe, which would in turn favor the creation of defects for prolonged reaction times. Fe^{2+} species might also be present. This would induce a shift of the spectra toward lower binding energies, however, which would signify a presence of Fe^{2+} mainly at medium reaction times, which seems unlikely. The shift toward higher binding energy after 30 min could in part also be caused by the extraction of copper, shifting the peaks toward those of Fe_3O_4.[60] Cu defects might likewise lead to a shift in the iron spectra toward higher binding energies.

A change in the degree of inversion is expected to correlate with changes in the conductivity and electrocatalysis,[19,37,63–65] and the magnetic properties.[19] A similar effect would result from the presence of defects. The agglomeration behavior of the nanoparticulate powder was visibly altered by the synthesis time: the agglomeration was especially pronounced for $CuFe_2O_4$ obtained at relatively short reaction times (5 and 10 min) and decreased with increasing reaction durations, in relation to a decrease in the degree of inversion, as also observable in DLS and ultracentrifugation measurements (Figure S14, Supporting Information). For $CuFe_2O_4$ with a synthesis time of 1 and 30 min—which are agglomerating least according to DLS measurements—particle diameters of 13 and 16 nm were obtained with the ultracentrifugation experiments, in good agreement to the sizes measured from TEM images. For more strongly agglomerating particles, a shoulder can be observed around 13 nm, but no accurate size determination is possible due to the pronounced agglomeration tendency.

2.2. Electrocatalytic CO_2 Reduction

We evaluated the influence of the synthesis parameters on the electrochemical CO_2RR of $CuFe_2O_4$ electrodes in 0.1 M $KHCO_3$ solutions, using an H-cell setup (Figure S15, Supporting Information). In order to determine the optimal potential, chronoamperometric measurements were performed at different potentials for exemplary electrodes of the sample synthesized for 15 min at 175 °C (Figure S16, Supporting Information). The evolved gases were examined after 20 and 60 min, respectively, to differentiate between the initial activation phase, during which high negative currents occur due to the decomposition of organic residues and possible activation of $CuFe_2O_4$, and the steady-state phase, for which the current response is stable. CO was the main C-product at all potentials, with the highest production rate at −0.8 V vs. RHE (**Figure 5**). The Faradaic efficiency and selectivity were best at lower potentials of −0.6 V due to hydrogen evolution taking over at highly reducing potentials. The Faradaic efficiency was lower than the selectivity, which is calculated from only the gaseous products, at all potentials, indicating the formation of other C-products, albeit to a rather low extent. The difference was especially high at low potentials, which is in good agreement to the lower required potentials for methane or methanol formation.[66] A potential of −0.7 V vs. RHE was chosen in the following, to evaluate differences in the catalytic performance of $CuFe_2O_4$

© 2023 The Authors. Advanced Energy and Sustainability Research published by Wiley-VCH GmbH

26999412, 2023, 4, Downloaded from https://onlinelibrary.wiley.com/doi/10.1002/aesr.202200184 by Universitaet Bayreuth, Wiley Online Library on [24/07/2023]. See the Terms and Conditions (https://onlinelibrary.wiley.com/terms-and-conditions) on Wiley Online Library for rules of use; OA articles are governed by the applicable Creative Commons License

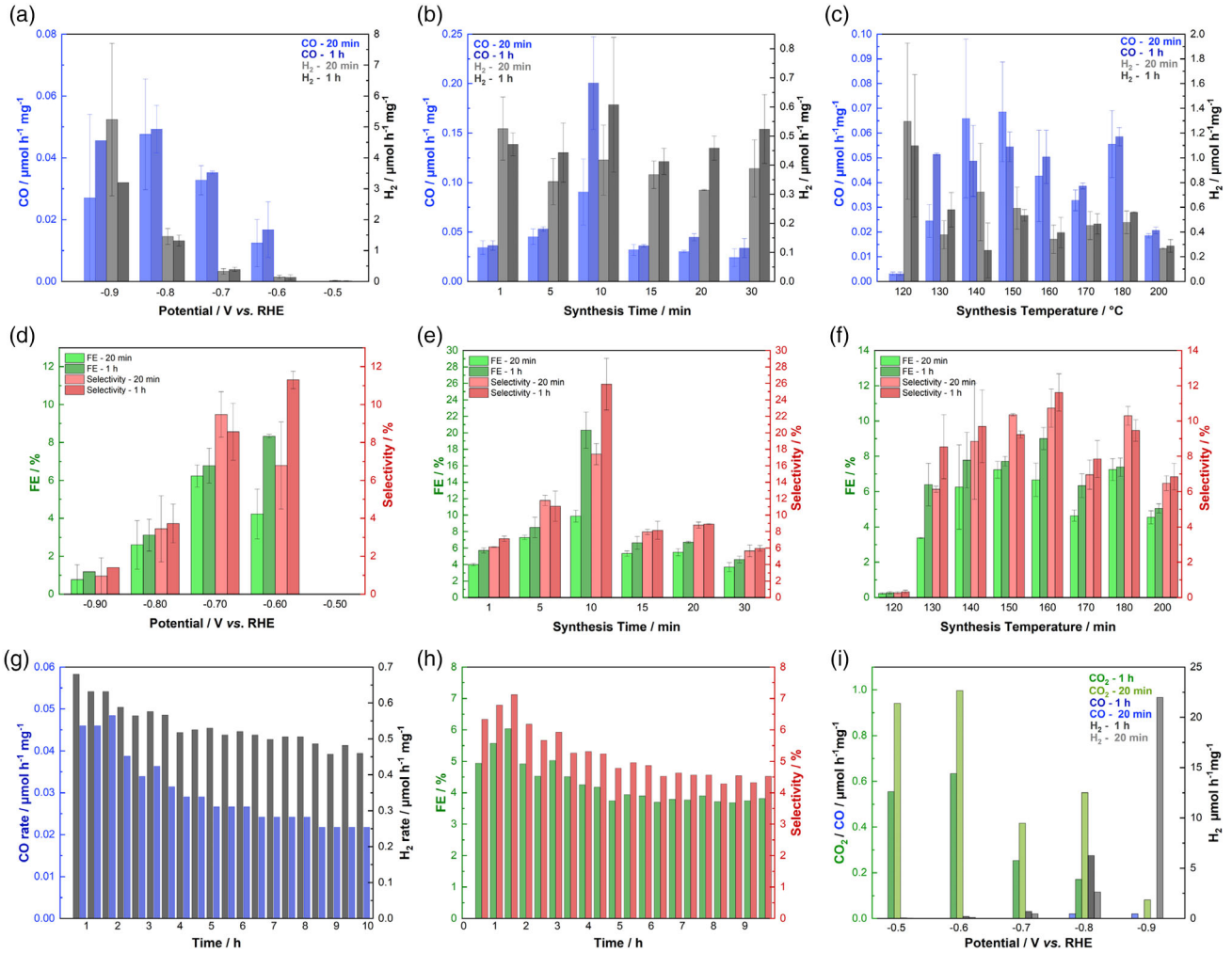

Figure 5. CO and H_2 production rates at a) different potentials for $CuFe_2O_4$ synthesized at 175 °C for 15 min, b) for $CuFe_2O_4$ synthesized at 175 °C obtained after different reaction times, and c) for $CuFe_2O_4$ synthesized for 15 min at different temperatures. Corresponding Faradaic efficiencies (FE) and selectivities for CO are shown in d) for different potentials with $CuFe_2O_4$ synthesized at 175 °C for 15 min, in e) with $CuFe_2O_4$ synthesized at 175 °C obtained after different reaction times, and in f) with $CuFe_2O_4$ synthesized for 15 min at different temperatures. The results for the long-time testing are shown in g,h). Comparative measurements in an Ar atmosphere solely yielded CO_2 and H_2 i). The performance evaluation at −0.9 V versus RHE was interrupted after 20 min due to high currents.

prepared under varying synthesis conditions. The measurements were performed at least twice with freshly prepared electrodes, to account for possible variations between measurements.

A maximum CO yield of 0.2 µmol h^{-1} mg^{-1} was observed for $CuFe_2O_4$ synthesized for 10 min in the microwave, with the CO production rate sharply decreasing for samples obtained after longer synthesis times. The hydrogen evolution rate was highly similar for all samples independent of the synthesis time of the catalyst, with three to ten times more hydrogen being produced compared to CO. The CO yield was higher after one hour of potential application, probably due to the initial decomposition of organic residues. The Faradaic efficiency was also better after one hour and highest for the sample obtained after 10 min of reaction time (Figure 5).

Again, the Faradaic efficiency was slightly lower than the calculated selectivity based on gas product analysis, indicating the generation of low amounts of additional liquid products. The difference in the observed activity and selectivity in dependence of time is probably based on two adverse effects. On the one hand, the relative mass of organic residues increases with decreasing reaction duration, as observed in TG-MS. Correspondingly, both activity and selectivity are lower for $CuFe_2O_4$ obtained after short synthesis times. In an adverse effect, the degree of inversion is decreasing with increasing reaction time. On the one hand, a decrease in the inversion parameter will result in an increased conductivity.[19] Additionally, the local environment of copper —again determined by the degree of inversion—can have an influence on the catalytic performance. At the highly negative potentials employed for the CO_2RR, $CuFe_2O_4$ is likely at least partially reduced similar to what has been reported for binary copper oxide materials. In the case of copper oxide, the morphology and composition of the initial CuO_x have been shown to have

© 2023 The Authors. Advanced Energy and Sustainability Research published by Wiley-VCH GmbH

26999412, 2023, 4, Downloaded from https://onlinelibrary.wiley.com/doi/10.1002/aesr.202200184 by Universitaet Bayreuth, Wiley Online Library on [24/07/2023]. See the Terms and Conditions (https://onlinelibrary.wiley.com/terms-and-conditions) on Wiley Online Library for rules of use; OA articles are governed by the applicable Creative Commons License

a significant influence on the activity and selectivity.[8,9,67–69] While some suggest that subsurface oxygen or residual Cu^{x+} species play a crucial role in the CO_2 reduction, others argue that copper is completely reduced under the employed conditions.[8,69] Therefore, the initial cation distribution and primary coordination of copper by four or six oxygen atoms, respectively, can also be expected to affect the performance of the catalyst, since it may influence the stability against reduction and the local environment (e.g., coordination number) of active copper species. For example, Acharya et al. observed a dependence of the performance of a $FeNiO(H)_x$ catalyst in electrochemical oxygen evolution on the coordination environment of Fe^{3+},[70] elucidating that the cation coordination environment and change thereof can have a significant influence on the activity in electrocatalysis.

Indeed, Cu^{2+} in the spinel can partially be reduced to Cu^0 as shown by CV measurements in Ar saturated Na_2SO_4 solution.[71,72] The reduction was, however, clearly not completed after one scan, since an evolution with time was observed, indicating that the process is taking several minutes. If the CV scans were performed on electrophoretic-deposited $CuFe_2O_4$ on FTO, a color change to black was observed that was changing back to normal after storage under air, or application of a positive potential (Figure S17, Supporting Information). XRD after the experiment shows the spinel structure, proving that the reduction is reversible, or restricted to the surface (Figure S17, Supporting Information). The same redox peaks are apparent in the CV scans performed before the CO_2RR experiments in CO_2 saturated $KHCO_3$, although the reduction peaks overlap with the highly negative current response for CO_2 reduction (Figure S18, Supporting Information). The CV after the CO_2RR still shows the same redox features, supporting the reversibility of the redox processes.

A correlation of the crystallite size and micro-strain of $CuFe_2O_4$ electrocatalysts prepared with different synthesis times with their activity and selectivity in the CO_2RR was also noted and might partially contribute to the observed trend, as both could affect conductivity. Si and K doping, as well as Cu extraction at prolonged reaction times, furthermore represents an increasing concentration of defects, which might alter the electronic and surface properties of $CuFe_2O_4$, resulting in a decreased activity.

Additionally, the CO_2RR experiment was performed on $CuFe_2O_4$ obtained at different temperatures. A highly similar activity was observed for samples synthesized at temperatures between 130 and 180 °C, even though the amount of organic residues and of Cu^+ species varied between samples. Both differences are small, however, for $CuFe_2O_4$ synthesized in this temperature range. The determined degree of inversion was additionally similar for all samples, supporting the dominant influence of this parameter on the activity. Only for $CuFe_2O_4$ prepared at very low synthesis temperature, i.e., 120 °C, the high amounts of organic residues, significant presence of surface Cu^+ species, and low crystallinity resulted in a markedly decreased CO production rate and FE. The CO production rate—and to a lesser extent also the FE—was additionally decreased for the sample obtained at 200 °C. This is likely due to the observed Cu_2O by-phase. Deviations in the amounts of Cu^+ observed in the XPS for samples obtained at different temperatures, apparently only had a negligible influence on the performance, likely because the coordination environment was similar and some reduction of copper proceeds anyway during the electrochemical measurement.

Gas evolution rates are also shown non-normalized in Figure S19, Supporting Information, exhibiting smaller deviations between measurements and a comparable activity between both studies. This is at least partially due to some of the catalyst ink diffusing underneath the Kapton tape, thus contributing to the apparent mass loading while not being in contact with the electrolyte.

Due to the presence of organic residues as observed in the DRIFT and TG-MS measurements and their apparent decomposition in the initial phase of the potential application, we performed a comparative experiment in argon atmosphere, to verify that the observed CO does not stem from organic adsorbates at the catalyst surface. Depending on the applied potential, CO_2 and H_2 were detected with the CO_2 to H_2 ratio highest at low overpotentials (Figure 5). The measured currents were significantly lower than that in a CO_2 atmosphere, supporting the CO_2 conversion to CO. Blank carbon paper electrodes only yielded low amounts of hydrogen and no CO (Figure S20, Supporting Information). The duration of the CO_2RR could be extended to several hours at −0.7 V vs. RHE, although the activity started to slightly decrease after two hours (Figure 5), as did the current response. Slow material changes might occur with time, such as a more prominent reduction of metal ions or possibly also cation redistribution. However, since no flow setup was used, a portion of the decrease might also simply be due to electrolyte decomposition and detachment of the catalyst from the carbon paper caused by gas bubble formation. These effects might be mitigated by an optimization of the electrode preparation that was not in the focus of this research. Still, the preliminary results exhibit the potential of $CuFe_2O_4$ as an electrocatalyst for the CO2RR. Even after the measurement for 10 h, no alcoholic products were found (Figure S21, Supporting Information). Thus, the CO_2 to CO reduction is highly selective, and while large amounts of hydrogen are produced alongside CO, this product composition can be beneficial for the subsequent use as syngas, e.g., in the Fischer–Tropsch process. XRD patterns were measured for $CuFe_2O_4$ on carbon paper before and after the electrocatalysis (Figure S22, Supporting Information). Mostly reflections corresponding to $CuFe_2O_4$ are visible after the electrocatalysis, proving the good stability/reversibility of occurring redox reactions in the material even at highly reducing potentials. After the CO2RR was conducted for 1 h at −0.9 V vs. RHE, additional minor reflections for Cu_2O were observed, indicating partial reduction of the material under operating conditions, in agreement to the observed color change during CV on FTO (Figure S17, Supporting Information) and to what is known for copper oxide-derived electrocatalysts.[8]

3. Conclusion

We successfully prepared $CuFe_2O_4$ nanoparticles with a cubic, partially inverted spinel structure via a fast, low-temperature aqueous approach. A crystalline product was obtained after only 1 min at 175 °C in a microwave-assisted synthesis. A prolonged reaction time resulted in a decrease of the inversion parameter, and only a slight increase in the particle size was observed. The

© 2023 The Authors. Advanced Energy and Sustainability Research published by Wiley-VCH GmbH

26999412, 2023, 4, Downloaded from https://onlinelibrary.wiley.com/doi/10.1002/aesr.202200184 by Universitaet Bayreuth, Wiley Online Library on [24/07/2023]. See the Terms and Conditions (https://onlinelibrary.wiley.com/terms-and-conditions) on Wiley Online Library for rules of use; OA articles are governed by the applicable Creative Commons License

application in electrochemical CO_2 to CO reduction was very selective for CO and hydrogen, and an optimum performance was observed for $CuFe_2O_4$ obtained after medium synthesis duration (10 min), in correlation to the highest crystallite size and a medium degree of inversion. Samples obtained after shorter synthesis times contained large amounts of organic residues adsorbed to the particle surface that likely impede the activity of the $CuFe_2O_4$ catalyst, while those obtained after 30 min exhibited a decreased copper content, likely due to defect induction during cation migration, that likewise diminish the catalytic performance. Moreover, the synthesis temperature could be tuned between 120 and 200 °C. Both the material properties (degree of inversion, crystallite, and particle size) and the electrochemical performance were largely independent of the temperature, although high amounts of surface Cu^+ and organic residues impeded the performance of the sample synthesized at only 120 °C, and very low amounts of a Cu_2O by-phase were observed for the one obtained at 200 °C. The mild reaction conditions and very good availability of the material constituents make $CuFe_2O_4$ a promising electrocatalyst for the sustainable production of syngas.

4. Experimental Section

Microwave-Assisted Synthesis of $CuFe_2O_4$: Chemicals were purchased from commercial providers and used without further purification. In a typical approach, 1 mmol of $Fe(NO_3)_3 \cdot 9\ H_2O$ (404 mg, Acros Organics +99%) and 0.5 mmol of $Cu(NO_3)_2 \cdot 3\ H_2O$ (120.8 mg, Acros Organics +99%) were dissolved in a mixture of ethylene glycol (Acros Organics, 99.5%) and water. The pH was adjusted to 12 with 3 M KOH solution under rigorous stirring in a borosilicate microwave vial. The vial was sealed and placed in the microwave reactor (Monowave 400, Anton Paar), where it was heated to the desired temperature as fast as possible under stirring at 800 rpm. After the specified time, the solution was cooled with compressed air to 55 °C. The $CuFe_2O_4$ particles were collected via centrifugation, washed thrice with water and once with ethanol, and dried overnight at 80 °C.

Characterization: As-synthesized $CuFe_2O_4$ samples were characterized with powder X-ray diffraction (XRD), using either a Malvern PANalytical Empyrean device with Cu K_α irradiation ($\lambda_1 = 1.5406$ Å; $\lambda_2 = 1.54443$ Å) with an acceleration voltage of 40 kV and an emission current of 40 mA, or a STOE STADI P Mythen2 4 K diffractometer with Ag $K_{\alpha1}$ irradiation ($\lambda = 0.5594$ Å), a Ge(111) monochromator and equipped with four Dectris MYTHEN2 R 1 K strip detectors.[73] For Cu-XRD measurements, a spinning sample holder and Bragg–Brentano geometry were used, while the Ag-XRD measurements were performed in transmission geometry with Hilgenberg capillaries (0.5 mm). For improved data quality, measurements with Ag irradiation were performed repeatedly and automatically accumulated. X'Pert Highscore plus was used for phase analysis. Rietveld refinement was performed using FullProf.[74] The instrumental resolution was determined with LaB_6 (NIST SRM 660c). A Thompson–Cox–Hastings pseudo-Voigt function was used for peak shape modeling, and the background was approximated by linear interpolation between manually added points.[75] Refined parameters are zero, scale, cell parameters, FWHM with focus on the Lorentz contribution and including asymmetry parameters and size anisotropy, isotropic B values, and occupation (using a half inverted structure as starting point). The crystallographic information published by Mahmood et al. was used for the refinement of $CuFe_2O_4$,[76] and the information provided by Kirfel et al. was employed for a Cu_2O by-phase if required.[77] The fitting procedure was repeated at least twice and depicted error bars represent the standard deviation between fits.

Transmission electron microscopy (TEM) was employed for the determination of sample morphology, size, and crystallinity, using a 200 kV JEOL JEM-2200FS EFTEM, equipped with a Schottky FEG and an omega in-column energy filter. Particle sizes were evaluated with ImageJ 1.53e. The morphology was additionally examined by scanning electron microscopy (SEM) that was performed on a Zeiss Leo 1530 device at an acceleration voltage of 3 kV after sputter coating with platinum (Cressington Sputter Coater 208 HR). The same instrument was used for energy-dispersive X-ray diffraction spectroscopy (EDX) using an acceleration voltage of 20 kV and an ultra-dry EDX detector by Thermo Fisher Scientific NS7.

X-ray photoelectron spectroscopy (XPS) was performed on a Physical Electronics PHI VersaProbe III Scanning XPS Microprobe instrument, using monochromatic Al K_α irradiation with a beam diameter of 100 µm. The beam voltage was set to 15 kV and the X-ray power to 25 W. Survey scans were recorded with a step size of 0.4 eV and step time of 50 ms at a pass energy of 224 eV. For high-resolution spectra, step size and time were set to 0.1 eV and 50 ms, respectively, using a pass energy of 26 eV. To avoid charging effects, samples were continuously flooded with electrons and Ar^+ ions at low energy. Data were evaluated with CASA XPS 2.3.17, using Shirley backgrounds and Gaussian–Lorentzian line shapes (GL30, except for Cu2O (GL80), based on the work of Biesinger).[61] For charge correction, the maximum of the Cu-$L_3M_{4,5}M_{4,5}$ Auger peak was fitted with the minimum required number of peaks and set to a kinetic energy of 917.7 eV.[61] For samples containing large amounts of surface Cu^+, the peak maximum was instead set to a kinetic energy of 916.8 eV. Fe 2*p* spectra were fitted with a doublet separation of 13.8 eV[78] and restricted area ratios of 2:1 for $2p_{3/2}$ to $2p_{1/2}$ in order to compensate for the overlap between Fe $2p_{3/2}$ and a minor Cu Auger $L_2M_{2,3}M_{2,3}$ signal. Furthermore, FWHM were set to identical for all Fe peak components within the $2p_{3/2}$ to $2p_{1/2}$ signals, respectively, but not identical for $2p_{3/2}$ and $2p_{1/2}$.[79]

For diffuse reflectance infrared Fourier transformed (DRIFT) spectroscopy, a Bruker Alpha II spectrometer and the software OPUS were used. For Raman measurements, a WITec alpha RA+ imaging system was employed, equipped with a UHTS 300 spectrometer and an Andor Newton 970 EMCCD camera. Diffuse-reflectance UV/vis measurements were performed on a Perkin Elmer Lambda 750 spectrometer, using a Praying Mantis (Harrick) and spectralon as white standard.

Dynamic light scattering measurements were performed on a Litesizer 500 instrument from Anton Paar, at a wavelength of 568 nm and 25 °C. Angle and focus were set to automatic. 5 mg of $CuFe_2O_4$ were dispersed in 20 mL of ultrapure water for 2 h using ultrasonication. For the calculation of the number weighed intensity distribution, an absorption coefficient of 0.1 m^{-1} and a refractive index of 2.5 were used, respectively. For particle size determination, a disc centrifuge DC24000 (CPS Instruments Inc.) was additionally used. Dispersions of 10 mg of sample in 1 mL of ultrapure H_2O were prepared via ultrasonification and 0.1 mL were injected at 24 k rpm. A density gradient was prepared using sucrose solutions. The same optical parameters as for DLS measurements were employed, and a PVC solution was used as a standard. For both DLS and ultracentrifugal experiments, measurements were repeated at least thrice.

For the characterization of specific surface area and gas adsorption properties, N_2 physisorption was performed on an Autosorb iQ-MP-MP-AG instrument (Anton Paar QuantaTec) at 77 K. Samples were degassed for 12 h at 120 °C prior to the measurements. For surface area calculation, the Brunauer–Emmet–Teller (BET) model was used, and the data were evaluated with ASiQwin. For pore-size distributions, the DFT model was used, treating the absorbent as silica.

Thermogravimetric analysis (TGA) with gas evolution detected via mass spectrometry (MS) was conducted with a Netzsch Jupiter STA 449C thermobalance and a Netzsch Aeolos QMS 402C quadrupole MS. The sample was heated to 850 °C in air, using a heating ramp of 5 K min^{-1}.

Electrochemical Experiments: The electrochemical CO_2 reduction (CO2RR) was performed in a two compartment cell, using CO_2 saturated 0.1 M aqueous $KHCO_3$ solution as the electrolyte and a three-electrode setup. Anolyte and catholyte compartments were separated by a Selemion AMV-N anion-exchange membrane (AGC group) and both were continuously purged with CO_2 gas from the bottom, with the flow rate for

© 2023 The Authors. Advanced Energy and Sustainability Research published by Wiley-VCH GmbH

26999412, 2023, 4, Downloaded from https://onlinelibrary.wiley.com/doi/10.1002/aesr.202200184 by Universitaet Bayreuth, Wiley Online Library on [24/07/2023]. See the Terms and Conditions (https://onlinelibrary.wiley.com/terms-and-conditions) on Wiley Online Library for rules of use; OA articles are governed by the applicable Creative Commons License

the working electrode compartment set to 20 mL min^{-1} (mass flow controller from Bronkhorst). A platinum counter electrode and Ag/AgCl reference electrode were employed for the measurement. For the preparation of the working electrode, 10 mg of $CuFe_2O_4$ was dispersed in 300 µL of *i*-propanol (p.a) and 20 µL of a 5 wt% Nafion solution (Alfa Aesar), using ultrasonication for minimum 1 h. Subsequently, 50 µL of the obtained catalyst ink was drop-cast onto carbon paper (Freudenberg H2315-C2) electrodes that were cut into 1 cm wide stripes. The exposed area was restricted to 1 cm^2 using Kapton tape. The electrodes were left to dry for at least one day in air. The electrolyte was purged with CO_2 (99.995 vol%, Air Liquide) for at least 10 min, prior to potential application. The internal resistance was checked and automatically corrected for prior to the actual experiment. A Gamry Reference 3000 potentiostat together with the software Gamry Framework was employed for all electrochemical measurements. The evolved gases were analyzed via gas chromatography (Shimadzu GC-2014, equipped with a HayeSep Q and a HayeSep R column in series, a thermal conductivity detector and a methanizer in series with a flame ionization detector (FID)) after 20 and 60 min. The potential was corrected to RHE with $V_{RHE} = V_{Ag/AgCl} + 0.209 + 0.059$*pH. For the reference measurement in Ar, the CO_2 gas was replaced by Ar at a flow rate of 20 mL min^{-1}. The pH change from 6.8 to 9.7 was taken into account for the conversion of the applied potential to RHE. Electrolyte from the working electrode compartment was sampled after the end of the experiment and analyzed with a liquid chromatograph (Shimadzu, GC-2030), equipped with a SH-Stabilwax column and FID, for the presence of alcohols and aldehydes. Faradaic efficiencies were calculated from the partial current for CO, or H_2, respectively, whereas selectivity calculations are based on the relative fraction of CO in gaseous products, i.e., H_2 and CO together. Cyclic voltammetry (CV) measurements in a CO_2 atmosphere were conducted with the same setup at a scan rate of 20 mV s^{-1}. For comparative measurements in 0.1 M Na_2SO_4, $CuFe_2O_4$ was deposited electrophoretically on a fluorine doped tin oxide (FTO) substrate. The CV scans were performed with a three-electrode setup in a PECC-2 cell (Zahner Elektrik), using platinum as a counter, Ag/AgCl as a reference, and the deposited sample on FTO as a working electrode, respectively, with the exposed area of the latter being restricted to 1 cm^2. A Zennium potentiostat (Zahner Elektrik) was used, and the scan rate was 20 mV s^{-1}.

Supporting Information

Supporting Information is available from the Wiley Online Library or from the author.

Acknowledgements

The authors thank Dr. Holger Schmalz (University of Bayreuth, Keylab Synthesis and Molecular Characterisation, Bavarian Polymer institute (BPI)) for Raman-AFM analysis, Lena Geiling (University of Bayreuth) for TG-MS measurements, and Christopher Simon (formerly University of Bayreuth) for TEM analysis. Furthermore, the authors are grateful to the BPI for the usage of XPS and SEM devices (KeyLabs Device Engineering and Electron and Optical Microscopy, respectively) and to Prof. Dr. Ing. Christina Roth and Hendrik Hoffmann (University of Bayreuth) for providing access to the CO_2-reduction setup and assistance during the measurements. The authors additionally thank Jonas Jungmann and Dr. Jana Timm for performing the physisorption measurements, as well as Micro Ade and Anja Hofmann for SEM and EDX analysis. Moreover, the authors thank Julia Woelfel and Teresa Mauerer for assistance in the lab. J.Z. and R.M. gratefully acknowledge funding in the graduate school of the Bavarian Center for Battery Technology (BayBatt), University of Bayreuth and by the Bavarian State Ministry of Science, Research and Arts within the collaborative research network Solar Technologies Go Hybrid.

Conflict of Interest

The authors declare no conflict of interest.

Data Availability Statement

The data that support the findings of this study are available from the corresponding author upon reasonable request.

Open Access funding enabled and organized by Projekt DEAL.

Keywords

CO_2 reduction, electrocatalyses, microwave syntheses, nanoparticles

Received: December 5, 2022
Revised: December 20, 2022
Published online: January 25, 2023

[1] Q. Lu, F. Jiao, *Nano Energy* **2016**, *29*, 439.
[2] B. Kumar, J. P. Brian, V. Atla, S. Kumari, K. A. Bertram, R. T. White, J. M. Spurgeon, *Catal. Today* **2016**, *270*, 19.
[3] J. P. Jones, G. K. S. Prakash, G. A. Olah, *Isr. J. Chem.* **2014**, *54*, 1451.
[4] S. Nitopi, E. Bertheussen, S. B. Scott, X. Liu, A. K. Engstfeld, S. Horch, B. Seger, I. E. L. Stephens, K. Chan, C. Hahn, J. K. Nørskov, T. F. Jaramillo, I. Chorkendorff, *Chem. Rev.* **2019**, *119*, 7610.
[5] Y. Zou, S. Wang, *Adv. Sci.* **2021**, *8*, 2003579.
[6] Y. Zhou, A. J. Martín, F. Dattila, S. Xi, N. López, J. Pérez-Ramírez, B. S. Yeo, *Nat. Catal.* **2022**, *5*, 545.
[7] W. Fu, Z. Liu, T. Wang, J. Liang, S. Duan, L. Xie, J. Han, Q. Li, *ACS Sustainable Chem. Eng.* **2020**, *8*, 15223.
[8] Y. Lum, J. W. Ager, *Angew. Chem., Int. Ed.* **2018**, *57*, 551.
[9] L. Mandal, K. R. Yang, M. R. Motapothula, D. Ren, P. Lobaccaro, A. Patra, M. Sherburne, V. S. Batista, B. S. Yeo, J. W. Ager, J. Martin, T. Venkatesan, *ACS Appl. Mater. Interfaces* **2018**, *10*, 8574.
[10] S. H. Lee, J. C. Lin, M. Farmand, A. T. Landers, J. T. Feaster, J. E. Avilés Acosta, J. W. Beeman, Y. Ye, J. Yano, A. Mehta, R. C. Davis, T. F. Jaramillo, C. Hahn, W. S. Drisdell, *J. Am. Chem. Soc.* **2021**, *143*, 588.
[11] A. M. Balagurov, I. A. Bobrikov, V. Y. Pomjakushin, D. V. Sheptyakov, V. Y. Yushankhai, *J. Magn. Magn. Mater.* **2015**, *374*, 591.
[12] M. Desai, S. Prasad, N. Venkataramani, I. Samajdar, A. K. Nigam, R. Krishnan, *J. Appl. Phys.* **2002**, *91*, 2220.
[13] R. S. Yadav, J. Havlica, J. Masilko, L. Kalina, J. Wasserbauer, M. Hajdúchová, V. Enev, I. Kuřitka, Z. Kožáková, *J. Supercond. Nov. Magn.* **2016**, *29*, 759.
[14] H. Ohnishi, T. Teranishi, *J. Phys. Soc. Jpn.* **1961**, *16*, 35.
[15] A. Yang, X. Zuo, L. Chen, Z. Chen, C. Vittoria, V. G. Harris, *J. Appl. Phys.* **2005**, *97*, 8.
[16] K. R. Sanchez-Lievanos, J. L. Stair, K. E. Knowles, *Inorg. Chem.* **2021**, *60*, 4291.
[17] X. Zuo, A. Yang, C. Vittoria, V. G. Harris, *J. Appl. Phys.* **2006**, *99*, 4.
[18] A. M. Balagurov, I. A. Bobrikov, M. S. Maschenko, D. Sangaa, V. G. Simkin, *Crystallogr. Rep.* **2013**, *58*, 710.
[19] R. Zhang, Q. Yuan, R. Ma, X. Liu, C. Gao, M. Liu, C. L. Jia, H. Wang, *RSC Adv.* **2017**, *7*, 21926.
[20] M. Yokoyama, A. Nakamura, T. Sato, K. Haneda, *J. Magn. Soc. Jpn.* **1998**, *22*, S1_243.
[21] S. Roy, J. Ghose, *J. Appl. Phys.* **2000**, *87*, 6226.
[22] R. Khunphonoi, P. Khemthong, C. Luadthong, S. Kuboon, C. Kongmark, N. Viriya-empikul, P. Kidkhunthod, S. Pinitsoontorn, K. Faungnawakij, *RSC Adv.* **2022**, *12*, 15526.

© 2023 The Authors. Advanced Energy and Sustainability Research published by Wiley-VCH GmbH

26999412, 2023, 4, Downloaded from https://onlinelibrary.wiley.com/doi/10.1002/aesr.202200184 by Universitaet Bayreuth, Wiley Online Library on [24/07/2023]. See the Terms and Conditions (https://onlinelibrary.wiley.com/terms-and-conditions) on Wiley Online Library for rules of use; OA articles are governed by the applicable Creative Commons License

[23] C. Reitz, C. Suchomski, J. Haetge, T. Leichtweiss, Z. Jagličić, I. Djerdj, T. Brezesinski, *Chem. Commun.* **2012**, *48*, 4471.
[24] M. Feng, A. Yang, X. Zuo, C. Vittoria, V. G. Harris, *J. Appl. Phys.* **2010**, *107*, 1025.
[25] S. Bera, S. Ghosh, T. Maiyalagan, R. N. Basu, *ACS Appl. Energy Mater.* **2022**, *5*, 3821.
[26] S. Park, J. H. Baek, L. Zhang, J. M. Lee, K. H. Stone, I. S. Cho, J. Guo, H. S. Jung, X. Zheng, *ACS Sustainable Chem. Eng.* **2019**, *7*, 5867.
[27] N. Guijarro, P. Bornoz, M. Prévot, X. Yu, X. Zhu, M. Johnson, X. Jeanbourquin, F. Le Formal, K. Sivula, *Sustainable Energy Fuels* **2018**, *2*, 103.
[28] Y. Liu, F. Le Formal, F. , L. Yao, K. Sivula, N. Guijarro, *J. Mater. Chem. A* **2019**, *7*, 1669.
[29] S. Tao, F. Gao, X. Liu, O. T. Sørensen, *Mater. Sci. Eng. B Solid-State Mater. Adv. Technol.* **2000**, *77*, 172.
[30] J. Zheng, Z. Lin, W. Liu, L. Wang, S. Zhao, H. Yang, L. Zhang, *J. Mater. Chem. B* **2014**, *2*, 6207.
[31] L. S. Ferreira, T. R. Silva, V. D. Silva, R. A. Raimundo, T. A. Simões, F. J. A. Loureiro, D. P. Fagg, M. A. Morales, D. A. Macedo, *Adv. Powder Technol.* **2022**, *33*, 103391.
[32] K. M. Rezaul Karim, M. Tarek, H. R. Ong, H. Abdullah, A. Yousuf, C. K. Cheng, M. M. R. Khan, *Ind. Eng. Chem. Res.* **2019**, *58*, 563.
[33] K. M. Rezaul Karim, H. R. Ong, H. Abdullah, A. Yousuf, C. K. Cheng, M. M. Rahman Khan, *Int. J. Hydrogen Energy* **2018**, *43*, 18185.
[34] M. R. Khan, M. R. Uddin, H. Abdullah, K. R. Karim, A. Yousuf, *Int. J. Chem. Mol. Nucl. Mater. Metall. Eng.* **2016**, *10*, 1273.
[35] R. Köferstein, T. Walther, D. Hesse, S. G. Ebbinghaus, *J. Solid State Chem.* **2014**, *213*, 57.
[36] T. Ramaprasad, R. J. Kumar, U. Naresh, M. Prakash, D. Kothandan, K. C. B. Naidu, *Mater. Res. Express* **2018**, *5*, 095025.
[37] C. Simon, M. B. Zakaria, H. Kurz, D. Tetzlaff, A. Blösser, M. Weiss, J. Timm, B. Weber, U. P. Apfel, R. Marschall, *Chem. - Eur. J.* **2021**, *27*, 16990.
[38] A. Bloesser, H. Kurz, J. Timm, F. Wittkamp, C. Simon, S. Hayama, B. Weber, U.-P. Apfel, R. Marschall, *ACS Appl. Nano Mater.* **2020**, *3*, 11587.
[39] C. Simon, A. Blösser, M. Eckardt, H. Kurz, B. Weber, M. Zobel, R. Marschall, *Z. Anorg. Allg. Chem.* **2021**, *647*, 2061.
[40] S. Komarneni, M. C. D'Arrigo, C. Leonelli, G. C. Pellacani, H. Katsuki, *J. Am. Ceram. Soc.* **1998**, *81*, 3041.
[41] E. Solano, L. Perez-Mirabet, F. Martinez-Julian, R. Guzmán, J. Arbiol, T. Puig, X. Obradors, R. Yañez, A. Pomar, S. Ricart, J. Ros, *J. Nanopart. Res.* **2012**, *14*, 1034.
[42] I. Bilecka, I. Djerdj, M. Niederberger, *Chem. Commun.* **2008**, 886.
[43] A. Phuruangrat, B. Kuntalue, S. Thongtem, T. Thongtem, *Mater. Lett.* **2016**, *167*, 65.
[44] R. Jalajerdi, D. Ghanbari, *J. Nanostruct.* **2016**, *6*, 278.
[45] T. G. Altincekic, I. Boz, A. Baykal, S. Kazan, R. Topkaya, M. S. Toprak, *J. Alloys Compd.* **2010**, *493*, 493.
[46] B. K. Chatterjee, K. Bhattacharjee, A. Dey, C. K. Ghosh, K. K. Chattopadhyay, *Dalt. Trans.* **2014**, *43*, 7930.
[47] M. D. P. Silva, F. C. Silva, F. S. M. Sinfrônio, A. R. Paschoal, E. N. Silva, C. W. A. Paschoal, *J. Alloys Compd.* **2014**, *584*, 573.
[48] R. D. Waldron, *Phys. Rev. B* **1955**, *99*, 1727.
[49] R. K. Selvan, C. O. Augustin, L. J. Berchmans, R. Saraswathi, *Mater. Res. Bull.* **2003**, *38*, 41.
[50] K. Shameli, M. Bin Ahmad, S. D. Jazayeri, S. Sedaghat, P. Shabanzadeh, H. Jahangirian, M. Mahdavi, Y. Abdollahi, *Int. J. Mol. Sci.* **2012**, *13*, 6639.
[51] M. T. Caccamo, S. Magazù, *Appl. Spectrosc.* **2017**, *71*, 401.
[52] R. Zhang, M. Liu, L. Lu, S. B. Mi, C. L. Jia, H. Wang, *RSC Adv.* **2016**, *6*, 100108.
[53] M. I. Díez-García, T. Lana-Villarreal, R. Gómez, *ChemSusChem* **2016**, *9*, 1504.
[54] A. Le Nestour, M. Gaudon, G. Villeneuve, R. Andriessen, A. Demourgues, *Inorg. Chem.* **2007**, *46*, 2645.
[55] K. Biramally, N. Pujari, S. Karidas, M. D. Shareefuddin, D. Sreenivasu, C. P. Vardhani, in *AIP Conf. Proc. 2019*, Nagpur, India **2014**, 030016.
[56] F. Rodríguez, D. Hernández, J. Garcia-Jaca, *Phys. Rev. B: Condens. Matter Mater. Phys.* **2000**, *61*, 16497.
[57] R. G. Kulkarni, V. U. Patil, *J. Mater. Sci.* **1980**, *15*, 2221.
[58] M. Fantauzzi, F. Secci, M. Sanna Angotzi, C. Passiu, C. Cannas, A. Rossi, *RSC Adv.* **2019**, *9*, 19171.
[59] T. Aghavnian, J. B. Moussy, D. Stanescu, R. Belkhou, N. Jedrecy, H. Magnan, P. Ohresser, M. A. Arrio, P. Sainctavit, A. Barbier, *J. Electron Spectrosc. Relat. Phenom.* **2015**, *202*, 16.
[60] A. P. Grosvenor, B. A. Kobe, M. C. Biesinger, N. S. McIntyre, *Surf. Interface Anal.* **2004**, *36*, 1564.
[61] M. C. Biesinger, *Surf. Interface Anal.* **2017**, *49*, 1325.
[62] M. C. Biesinger, B. P. Payne, A. P. Grosvenor, L. W. M. Lau, A. R. Gerson, R. S. C. Smart, *Appl. Surf. Sci.* **2011**, *257*, 2717.
[63] Y. Zhou, Y. Du, S. Xi, Z. J. Xu, *Electrocatalysis* **2018**, *9*, 287.
[64] Y. Zhou, S. Sun, C. Wei, Y. Sun, P. Xi, Z. Feng, Z. J. Xu, *Adv. Mater.* **2019**, *31*, 1902509.
[65] M. Harada, F. Kotegawa, M. Kuwa, *ACS Appl. Energy Mater.* **2022**, *5*, 278.
[66] S. Chandrasekaran, C. Bowen, P. Zhang, Z. Li, Q. Yuan, X. Ren, L. Deng, *J. Mater. Chem. A* **2018**, *6*, 11078.
[67] J. Xie, Y. Huang, H. Yu, *Front. Environ. Sci. Eng.* **2015**, *9*, 861.
[68] J. J. Velasco-Vélez, C. H. Chuang, D. Gao, Q. Zhu, D. Ivanov, H. S. Jeon, R. Arrigo, R. V. Mom, E. Stotz, H. L. Wu, T. E. Jones, B. Roldan Cuenya, A. Knop-Gericke, R. Schlögl, *ACS Catal.* **2020**, *10*, 11510.
[69] T. C. Chou, C. C. Chang, H. L. Yu, W. Y. Yu, C. L. Dong, J. J. Velasco-Vélez, C. H. Chuang, L. C. Chen, J. F. Lee, J. M. Chen, H. L. Wu, *J. Am. Chem. Soc.* **2020**, *142*, 2857.
[70] P. Acharya, R. H. Manso, A. S. Hoffman, S. I. P. Bakovic, L. Kekedy-Nagy, S. R. Bare, J. Chen, L. F. Greenlee, *ACS Catal.* **2022**, *12*, 1992.
[71] S. D. Giri, A. Sarkar, *J. Electrochem. Soc.* **2016**, *163*, H252.
[72] F. Caballero-Briones, J. M. Artés, I. Díez-Pérez, P. Gorostiza, F. Sanz, *J. Phys. Chem. C* **2009**, *113*, 1028.
[73] S. L. J. Thomae, N. Prinz, T. Hartmann, M. Teck, S. Correll, M. Zobel, *Rev. Sci. Instrum.* **2019**, *90*, 043905.
[74] J. Rodrígues-Carvajal, *Phys. B Phys. Condens. Matter* **1993**, *192*, 55.
[75] P. Thompson, D. E. Cox, J. B. Hastings, *J. Appl. Cryst.* **1987**, *20*, 79.
[76] S. Briceño, H. Del Castillo, V. Sagredo, W. Bramer-Escamilla, P. Silva, *Appl. Surf. Sci.* **2012**, *263*, 100.
[77] A. Kirfel, K. Eichhorn, *Acta Crystallogr.* **1990**, *A46*, 271.
[78] P. Mills, J. L. Sullivan, *J. Phys. D. Appl. Phys.* **1983**, *16*, 723.
[79] J. F. Moulder, W. F. Stickle, P. E. Sobol, K. D. Bomben, in *Handbook of X-ray Photoelectron Spectroscopy* (Ed: J. Chastain), Perkin-Elmer Corporation, Minnesota **1993**.

© 2023 The Authors. Advanced Energy and Sustainability Research published by Wiley-VCH GmbH

26999412, 2023, 4, Downloaded from https://onlinelibrary.wiley.com/doi/10.1002/aesr.202200184 by Universitaet Bayreuth, Wiley Online Library on [24/07/2023]. See the Terms and Conditions (https://onlinelibrary.wiley.com/terms-and-conditions) on Wiley Online Library for rules of use; OA articles are governed by the applicable Creative Commons License